JOURNAL OF AIRCRAFT
Vol. 39, No. 6, November–December 2002

Rapid Transonic Aerodynamic Prediction for Hypersonic Lifting Bodies

Timothy F. O'Brien* and Mark J. Lewis†
University of Maryland, College Park, Maryland 20742

A rapid analytical method for predicting the transonic pressure distribution on high-speed, waverider-based, vehicle fuselages is presented. The goal of this method is the prediction of inviscid lift and drag using minimal CPU time. The method is based on the solution of the two-dimensional and axisymmetric transonic, small disturbance, velocity potential equations. Comparison is made between theory and the matching inviscid, three-dimensional, computational solution over a representative vehicle geometry. For purely subsonic flow, the methodology predicts lift, drag, and thrust on the lower surface to within 0.5, 1.1, and 0.5%, respectively, compared to the computational solution. For sonic flow, the methodology predicts lift, drag, and thrust on the lower surface to within 4.7, 5.1, and 9.5%, respectively, compared to the computational solution. For purely supersonic flow, the methodology predicts lift, drag, and thrust on the lower surface to within 7.4, −1.6, and −4.4%, respectively, compared to the computational solution. The analytical and computational analyses showed that this class of vehicle geometry generates little lift at low-speed and will require lift augmentation.

Nomenclature

C	=	Euler's constant
C_p	=	pressure coefficient
c	=	chord length, m
D	=	normalized drag, m^2
f	=	supersonic function
h	=	height, m
k	=	$M_\infty^2(\gamma+1)$
L	=	length of geometry, m; normalized lift, m^2
M_∞	=	freestream Mach number
n	=	exponent for solution combination
p	=	pressure, N/m^2
R	=	radius of curvature, m
r	=	coordinate in radial direction, m
S	=	cross-sectional area, m^2
T	=	normalized thrust, m^2
t	=	maximum thickness, m
U_∞	=	freestream velocity, m/s
u	=	perturbation velocity, m/s
$\bar{u}$	=	nondimensionalized perturbation velocity
x	=	direction along longitudinal axis of body, m
y	=	body ordinate in two dimensions, m
Z	=	body ordinate in radial coordinates, m
γ	=	ratio of specific heats
ξ	=	dummy variable of integration
τ	=	thickness ratio (t/c)
ϕ	=	perturbation velocity potential

Subscripts

2D	=	two-dimensional solution
axi	=	axisymmetric solution
end	=	ending point of geometry
h	=	hyperbolic
i	=	incompressible
loc	=	local
max	=	maximum
r	=	differentiation in the radial direction
sp	=	result of solution combination
st	=	starting point of geometry
x	=	differentiation in the x direction
xs	=	intersection point of spline
z	=	differentiation in the z direction

Superscripts

$'$	=	differentiation
$*$	=	sonic location

Received 15 July 2001; revision received 13 August 2002; accepted for publication 13 August 2002.

*Graduate Research Assistant, Department of Aerospace Engineering; currently Specialist Engineer, Hypersonic Design and Application, The Boeing Company, P.O. Box 516, MC S106-7250, St. Louis, MO, 63166-0516; timothy.f.o'brien@boeing.com. Member AIAA.

†Professor, Department of Aerospace Engineering; lewis@eng.umd.edu. Associate Fellow AIAA.

Introduction

THE design of an airbreathing, engine–airframe integrated vehicle capable of reaching hypersonic velocities and/or access to space will rely on the accurate prediction of the vehicle performance throughout the entire Mach number regime. The ultimate selection of an optimal hypersonic configuration may depend strongly on its low-speed performance, for takeoff and landing, as well as its ability to pass through the transonic regime. To this end, it is important to be able to analyze low-speed performance of a hypersonic craft.

Thorough investigations of the on-design performance of waverider-derived, airbreathing, engine–airframe integrated vehicles have been performed for configurations based on caret-wing waveriders,[1] conical waveriders,[2] osculating cone waveriders,[3] and wedge-based waveriders for missile application.[4] A scramjet engine was used as the main propulsion device for all of these vehicle studies. Because scramjets only operate at high speeds, these studies did not investigate the low-speed characteristics of waverider-based configurations.

The methodology developed herein would have application to the general class of slender airbreathing hypersonic craft. Where an example is required, the current study focuses on a representative baseline hypersonic vehicle that incorporates a rocket-based combined-cycle (RBCC) engine into an osculating cone, waverider-based, engine–airframe integrated vehicle. An RBCC engine has been chosen because of its ability to provide thrust across a wide Mach spectrum; a waverider shape has been selected because of the promise of high aerodynamic efficiency at high speeds. This class of

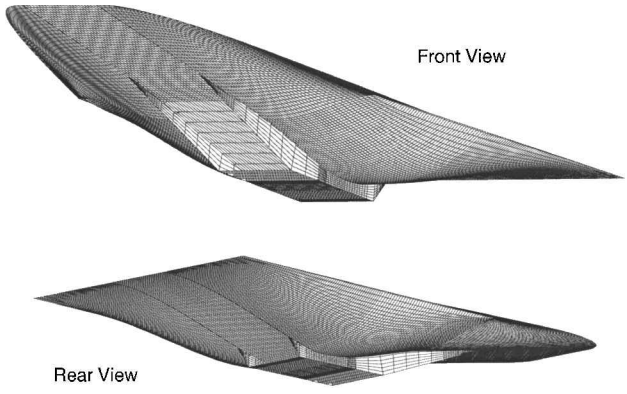

Fig. 1 Two views of example vehicle geometry, $M_\infty = 10$.

vehicle has been thoroughly studied for its on-design performance, and off-design supersonic flight.

An example of the class of vehicle geometries[5,6] of interest is shown in Fig. 1 for a design Mach number of 10. (Details of the methods used to develop these geometries may be found in Ref. 6.) The RBCC engine uses rockets to propel the vehicle from takeoff through the transonic regime, a ramjet to travel through the supersonic regime, a scramjet to travel through the hypersonic regime, and then a rocket to travel into orbit. Thus, the RBCC engine–airframe integrated concept has the potential to travel from takeoff to orbit in one stage, requiring knowledge of the off-design performance over the full Mach number range.

Previous investigations of the current vehicle class[5,6] calculated the hypersonic, off-design performance of a Mach 12 vehicle, for both Mach number and angle of attack, in the flight regime where scramjet propulsion was feasible, $M_\infty > 7$. A strong emphasis was placed on aerodynamic solutions that are computationally inexpensive (on the order of CPU seconds on a typical workstation). This will enable future initial design studies, optimizations, and/or trajectory analyses to be performed quickly and inexpensively.

For the current study, the inviscid, transonic, aerodynamic performance of a waverider-based, hypersonic fuselage (engine removed) is predicted analytically. Emphasis is placed on computationally inexpensive methods with CPU times on the order of 10 s or less. This restriction eliminates the use of computational fluid dynamics (CFD) solutions of the Euler or Navier–Stokes equations, where CPU times (neglecting grid generation) are typically in the minutes to hours range for a single vehicle design. Previous investigations into the low-speed and transonic behavior of waverider-based vehicles relied heavily on CFD solutions[7,8] and/or experimental methods.[9–11]

Several available analytical methods exist for predicting the transonic flow over certain geometries. Hodograph methods,[12,13] for example, have been used extensively, but are difficult to apply to these geometries because of the necessary transformation of the profile into the hodograph plane. Among the quickest and simplest methods is the solution of the small perturbation potential equations for transonic flow, on which this present effort is based. In particular, the Spreiter and Alksne method of local linearization[14,15] is used here to solve the two-dimensional and axisymmetric small-perturbation potential equations. The method of local linearization reduces the two-dimensional equations to analytical expressions and the axisymmetric equations to ordinary integro–differential equations, which may be numerically integrated very quickly. The two-dimensional and axisymmetric solutions are then combined together and compared to an Euler solution over the full three-dimensional vehicle. The ultimate goal has been the development of a rapid, transonic, aerodynamic prediction of the pressure distribution on a waverider-based, high-speed geometry for calculating inviscid lift and drag.

Two-Dimensional Transonic Flow Solution

The transonic, small-disturbance equation in two dimensions[14] may be written as

$$\left\{1 - M_\infty^2 - M_\infty^2[(\gamma+1)/U_\infty]\phi_x\right\}\phi_{xx} + \phi_{zz} = 0 \qquad (1)$$

Note that this equation simplifies to the linearized perturbation velocity potential equation if the coefficient of ϕ_x is neglected. However, this coefficient must be retained in the transonic equation to remain of mixed type (hyperbolic, parabolic, or elliptic). The governing equation is seen to change types according to the coefficient of ϕ_{xx},

$$1 - M_\infty^2 - M_\infty^2\frac{\gamma+1}{U_\infty}\phi_x \begin{cases} < 0 & \text{hyperbolic} \\ = 0 & \text{parabolic} \\ > 0 & \text{elliptic} \end{cases} \qquad (2)$$

Hence, Eq. (1) mimics the properties of transonic flow (flow where transition from subsonic to supersonic occurs). The solution of Eq. (1) may then be used to calculate the local pressure coefficient

$$C_p = -2(\phi_x/U_\infty) = -2(u/U_\infty) = -2\bar{u} \qquad (3)$$

where u is the perturbation velocity in the x direction.

The method of solution of the two-dimensional, transonic, small-disturbance equation selected for use in this study is the local linearization technique developed by Spreiter and Alksne.[14] A summary of the technique presented in Ref. 14. is provided in Ref. 6 for the solution of flows that are purely supersonic, purely subsonic, and near sonic. For a detailed discussion of the solutions, see Ref. 14.

Supersonic Solution

When the assumptions and methods of Ref. 14 are used, the supersonic solution of Eq. (1) yields the following algebraic equation for pressure coefficient:

$$C_p = \frac{2}{M_\infty^2(\gamma+1)}\left\{\left(M_\infty^2-1\right) - \left[\left(M_\infty^2-1\right)^{\frac{3}{2}} - \frac{3}{2}M_\infty^2(\gamma+1)\frac{\mathrm{d}Z}{\mathrm{d}x}\right]^{\frac{2}{3}}\right\} \qquad (4)$$

where k is defined as

$$k = M_\infty^2(\gamma+1) \qquad (5)$$

Note that the quantity in brackets should be positive. However, for solutions where the term does become negative, the minus sign in front of the bracket may be exchanged with a positive sign (and the absolute value of the bracket term taken) to predict the trend properly, albeit at the cost of increased solution error. It is also possible to assume that the pressure coefficient remains constant in this region (unless the term is negative at the leading edge of the vehicle, in which case a subsonic solution is more applicable).

Subsonic Solution

When the assumptions and methods of Ref. 14 are used, the subsonic solution of Eq. (1) yields the following integral equation for pressure coefficient:

$$C_p = -\left[2/M_\infty^2(\gamma+1)\right]\left\{\left(1-M_\infty^2\right) - \left[\left(1-M_\infty^2\right)^{\frac{3}{2}} + \tfrac{3}{4}M_\infty^2(\gamma+1)C_{p_i}\right]^{\frac{2}{3}}\right\} \qquad (6)$$

where C_{p_i} is the incompressible pressure coefficient found from

$$C_{p_i} = -\frac{2}{\pi}\int_{x_{\mathrm{st}}}^{x_{\mathrm{end}}}\left[\frac{\mathrm{d}Z}{\mathrm{d}\xi}\Big/(x-\xi)\right]\mathrm{d}\xi \qquad (7)$$

where x_{st} and x_{end} are the starting and ending points of the section to be analyzed. The second quantity in brackets in Eq. (6) must be positive. The same approach used in the supersonic solution to deal with any negative quantities may be applied to this case as well.

Near Sonic Solution

When the assumptions and methods of Ref. 14 are used, the near sonic solution of Eq. (1) yields the following differo–integral equation for pressure coefficient:

$$C_p = -\frac{2\left(1 - M_\infty^2\right)}{M_\infty^2(\gamma+1)} - 2\left\{\frac{3}{\pi M_\infty^2(\gamma+1)}\int_{x^*}^{x}\left[\frac{\mathrm{d}}{\mathrm{d}x_1}\int_{x_{\mathrm{st}}}^{x_1}\right.\right.$$

$$\left.\left.\times\left(\frac{\mathrm{d}Z}{\mathrm{d}\xi}\Big/\sqrt{x_1-\xi}\right)\mathrm{d}\xi\right]^2\mathrm{d}x_1\right\}^{\frac{1}{3}} \tag{8}$$

where x_1 is a dummy integration variable and x^* is the sonic location found by solving the following equation for x:

$$\frac{\mathrm{d}}{\mathrm{d}x}\int_{x_{\mathrm{st}}}^{x}\left(\frac{\mathrm{d}Z}{\mathrm{d}\xi}\Big/\sqrt{x-\xi}\right)\mathrm{d}\xi = 0 \tag{9}$$

For the sonic cases, it was observed that the near-nose region of the flowfield had a pressure distribution similar to that of a subsonic flow. Hence, the subsonic solution just shown is spline fit into the sonic solution at an applicable location along the body. The spline is performed by changing the constant of integration so that the sonic and subsonic solution are equal at the selected point. The solution to the pressure coefficient in the splined region is then

$$C_p = \frac{2}{M_\infty^2(\gamma+1)}\left\{\left[\left|1 - M_\infty^2 + \frac{M_\infty^2(\gamma+1)C_{p_{\mathrm{xs}}}}{2}\right|^{\frac{3}{2}}\right.\right.$$

$$\left.\left.+\frac{3}{4}M_\infty^2(\gamma+1)\left(C_{p_i} - C_{p_{i,\mathrm{xs}}}\right)\right]^{\frac{2}{3}} - \left(1 - M_\infty^2\right)\right\} \tag{10}$$

where subscript xs is the value at the subsonic/sonic solution intersection point.

Axisymmetric Transonic Flow Solution

The axisymmetric, small-disturbance, transonic, potential equation[15] is

$$\left(1 - M_\infty^2\right)\phi_{xx} + (1/r)\phi_r + \phi_{rr} = (k/U_\infty)\phi_x\phi_{xx} \tag{11}$$

The solution of Eq. (11) may be used to calculate the local pressure coefficient on the surface of the body,

$$C_p = -2\bar{u} - \left(\frac{\mathrm{d}Z}{\mathrm{d}x}\right)^2 \tag{12}$$

This work has used the axisymmetric local linearization technique developed by Spreiter and Alksne to solve the axisymmetric, small-disturbance, transonic, velocity potential equation.[15] Along with the two dimensional method, a summary of the solutions using this axisymmetric method for purely supersonic, purely subsonic, and near sonic is presented in Ref. 6. A detailed discussion of the derivation of the following equations may be found in Ref. 15.

Supersonic Solution

When the assumptions and methods of Ref. 15 are used, the supersonic solution of Eq. (11) yields the following nonlinear, ordinary differential–integral equation for nondimensionalized perturbation velocity:

$$\frac{\mathrm{d}\bar{u}}{\mathrm{d}x} = \frac{S'''(x)}{4\pi}\ell_n\left(\left|M_\infty^2 - 1 + k\bar{u}\right|\right) + \frac{\mathrm{d}f_h}{\mathrm{d}x} \tag{13}$$

where the absolute value of the natural logarithmic term is used to guarantee a positive value and f_h is

$$f_h(x) = \frac{S''(x)}{4\pi}\ell_n\left[\frac{S(x)}{4\pi x^2}\right] + \frac{1}{2\pi}\int_{x_{\mathrm{st}}}^{x}\frac{S''(x) - S''(\xi)}{x-\xi}\,\mathrm{d}\xi \tag{14}$$

This equation may be integrated numerically to solve for the nondimensional perturbation velocity $\bar{u}$ using a standard ordinary differential equation solver. For the present study, all ordinary differential equations (ODEs) are solved using the fourth-order Runge–Kutta scheme (see Ref. 16). To solve for the axisymmetric perturbation velocity for all three flow regimes, the geometries must be smooth to at least the third derivative [see Eq. (13)]. If this is not the case, large deviations in the second and third derivatives may cause significant errors.

To begin the solution of Eq. (13), a starting value for $\bar{u}$ must be specified at some x location. In the supersonic case, this point is found by solving for $S''(x) = 0$ (see Ref. 15). The corresponding perturbation velocity is then

$$\bar{u} = f_h \tag{15}$$

Solution then proceeds by starting at the derived location and marching forward and backward to cover the complete length of the body. Another starting point that may be selected for a purely supersonic solution is to calculate the pressure coefficient at the leading edge using the Taylor–Maccoll equation for supersonic flow over a cone. From the pressure coefficient, the starting value for $\bar{u}$ is found, the ODE is solved from the leading to the trailing edge. One final starting point (for sharp, cusped, trailing edges) is to set the pressure coefficient at the trailing edge to zero. This assumption may be used because the flow is assumed to be isentropic for the perturbation equations. All three of these starting points are used in the supersonic solution to follow.

Subsonic Solution

When the assumptions and methods of Ref. 15 are used, the subsonic solution of Eq. (11) yields the following nonlinear, ordinary differential–integral equation for nondimensionalized perturbation velocity:

$$\frac{\mathrm{d}\bar{u}}{\mathrm{d}x} = \frac{S'''(x)}{4\pi}\ell_n\left(\left|1 - M_\infty^2 - k\bar{u}\right|\right) + \frac{\mathrm{d}\bar{u}_i}{\mathrm{d}x} \tag{16}$$

where the absolute value of the natural logarithmic term is used to guarantee a positive value and $\bar{u}_i$ is the incompressible perturbation velocity found from

$$\bar{u}_i = \frac{S''(x)}{4\pi}\ell_n\frac{S(x)}{4\pi x(x_{\mathrm{end}} - x)} + \frac{1}{4\pi}\int_{x_{\mathrm{st}}}^{x_{\mathrm{end}}}\frac{S''(x) - S''(\xi)}{|x-\xi|}\,\mathrm{d}\xi \tag{17}$$

The initial point of solution is found by finding the value of x that satisfies $S''(x) = 0$ and then finding the value of $\bar{u} = \bar{u}_i$ at x (Ref. 15). Another starting point for the solution is to assume that the pressure coefficient at the trailing edge is zero (same reasoning as the supersonic solution) and to iterate the solution from trailing edge to leading edge. Both of these methods are employed in the solutions to follow.

Near Sonic Solution

When the assumptions and methods of Ref. 15 are used, the near sonic solution of Eq. (11) yields the following nonlinear, ordinary differential–integral equation for nondimensionalized perturbation velocity:

$$\frac{\mathrm{d}\bar{u}}{\mathrm{d}x} = \frac{S'(x)S''(x)}{4\pi S(x)} + \exp\left\{\frac{4\pi}{S''(x)}\left[\bar{u} + \frac{M_\infty^2 - 1}{M_\infty^2(\gamma+1)}\right.\right.$$

$$-\frac{S''(x)}{4\pi}\ell_n\left(\frac{M_\infty^2(\gamma+1)S(x)e^C}{4\pi x}\right)$$

$$\left.\left.-\frac{1}{4\pi}\int_{x_{\mathrm{st}}}^{x}\frac{S''(x) - S''(\xi)}{x-\xi}\,\mathrm{d}\xi\right]\right\} \tag{18}$$

where $C = 0.577215\ldots$ is Euler's constant. Solution of Eq. (18) requires a starting point, which is found by solving for the point at which $S''(x) = 0$. However, when $S''(x) = 0$ in Eq. (18), the solution is singular. Details of the determination of the initial solution point are discussed in Ref. 15. Spreiter and Alksne[15] also describe how the pressure distribution over the entire geometry may not be found using Eq. (18) alone. The sonic solution is splined to the supersonic and subsonic solutions (where applicable) to get the best solution. See Ref. 15 and the following sections for details.

Application of Local Linearization Technique to Prescribed Geometries

A demonstration of the applicability of the local linearization method for two-dimensional and axisymmetric flow will now be shown by comparing the theoretical results derived earlier to computational calculations and experimental findings. Two geometries are investigated: a parabolic arc of the form

$$Z = 2\tau c[x/c - (x/c)^2] \tag{19}$$

and a geometry similar to the centerline of the compression region of the example in Fig. 1. The profiles solved are shown in Fig. 2, where the parabolic arc has a thickness ratio of $\frac{1}{10}$, the centerline geometry (labeled cubic) has a thickness ratio of under 0.13, and flow goes from left to right.

The cubic centerline geometry is composed of a linear front section followed by two cubic polynomials. The cubic sections are joined so that the slopes remain continuous at the intersection points. The intersection points of each of these sections are shown in Fig. 2. As noted in the solution of the axisymmetric equations, the assumption of a smooth profile, that is, continuous derivatives in cross-sectional area, to the third derivative are necessary for a solution. However, when the original vehicle geometry[17] was developed in 2000, interest was only paid to a continuous first derivative in the cross section. Hence, to use the theory developed, a seventh-order spline (the lowest order to guarantee continuous third derivatives along the entire profile) was placed around the intersection points noted in Fig. 2. Each spline had a length of approximately 10% of the length of the vehicle and produced no noticeable difference in appearance of the shape. The third derivative of cross-sectional area of the original shape and the shape with the seventh-order spline are shown in Fig. 3. With the spline, the third derivative in cross-sectional area is continuous, but has a wide variation in value over a small distance. This will result in errors for the prediction of the perturbation velocity for the axisymmetric cases.

Two-Dimensional Results

The local linearization method in two dimensions was applied to the parabolic-arc airfoil described in Eq. (19) and the cubic centerline shape. The supersonic, subsonic, and sonic pressure distributions are shown in Figs. 4, 5, and 6, respectively, where the common airfoil nomenclature of negative pressure coefficient in the positive y direction is used. Also plotted in Figs. 4–6 are computational results calculated using the TURNS code.[18] TURNS uses a thin-layer approximation to the Navier–Stokes equations, using the Baldwin–Lomax turbulence model[19] to simulate turbulence. The

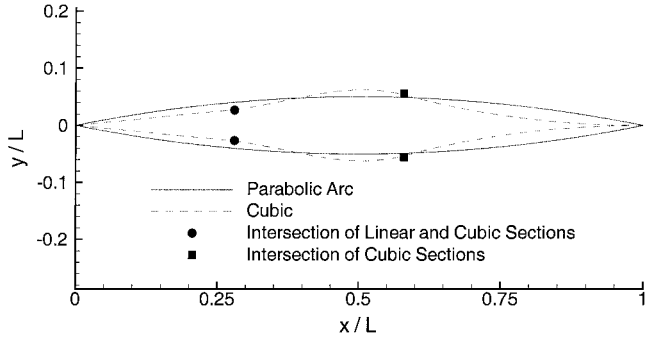

Fig. 2 Profiles of geometries solved for validation.

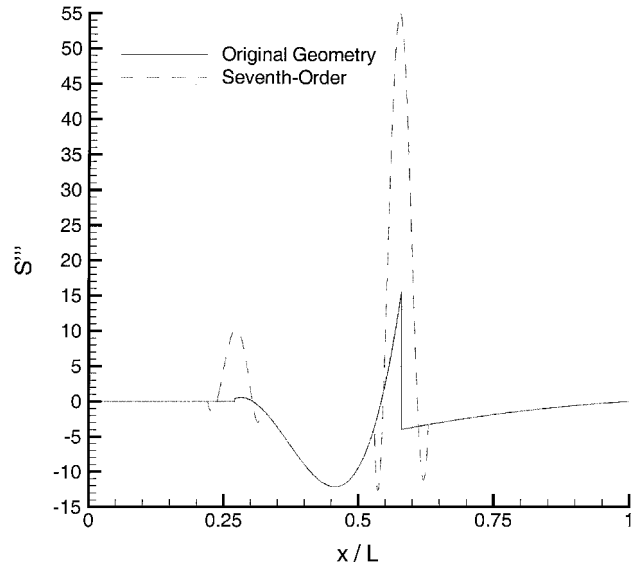

Fig. 3 Triple derivative of cross-sectional area for original geometry and seventh-order spline addition.

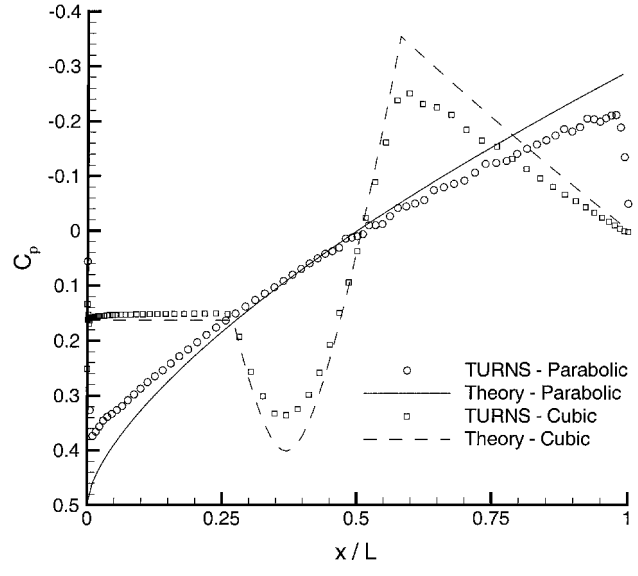

Fig. 4 Supersonic pressure distribution on parabolic airfoil, M_∞ = 1.57, and cubic airfoil, M_∞ = 1.65.

hyperbolic computational grid used had 217 points in the streamwise wraparound direction (including 74 in the wake region) and 91 points in the normal direction. The grid was extended a length of 20 vehicle lengths in all directions from the surface of the geometry. All viscous solutions were solved with a turbulent Reynold's number of 6×10^6. The viscous solutions are provided as a worst-case scenario for comparison to the inviscid, theoretical results.

Along with the full airfoil profile, for the subsonic and transonic solutions, a half-airfoil profile is solved. The half-airfoil profile is the same as the full airfoil, except that the top half of the airfoil is cut off, leaving a flat surface. This geometry was solved numerically to demonstrate the effects of the upper surface on the lower surface aerodynamics and to emulate the relatively flat surface of the example vehicle geometry.

A supersonic solution is shown in Fig. 4 for a Mach number of 1.57 for the parabolic arc and 1.65 for the cubic centerline. These Mach numbers correspond to roughly the upper critical Mach number on the geometries. Plotted in Fig. 4 are the viscous, computational solutions from TURNS along with the theoretical results (labeled theory). For the parabolic-arc airfoil, the theoretical results deviate from the computational results "near" the leading and trailing edges with errors of 23 and 30%, respectively. (Grid resolution

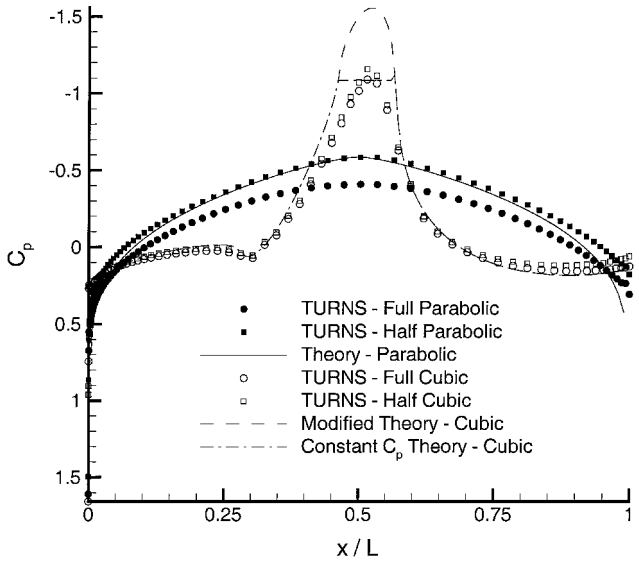

Fig. 5 Subsonic pressure distribution on parabolic airfoil, $M_\infty = 0.76$, and cubic airfoil, $M_\infty = 0.65$.

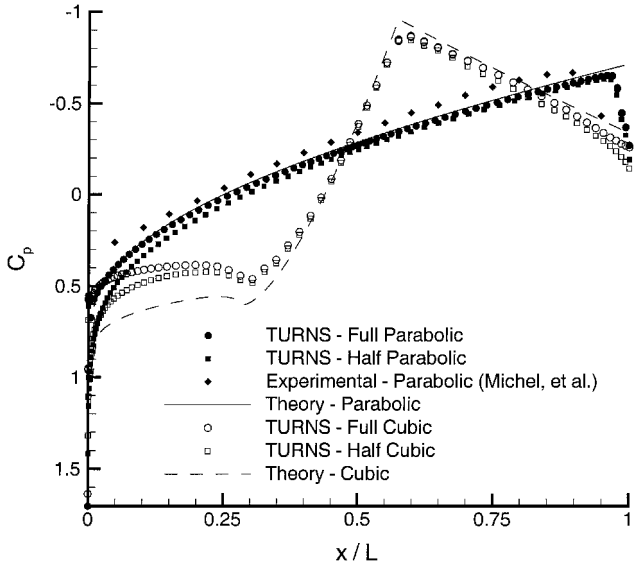

Fig. 6 Sonic pressure distribution on parabolic and cubic airfoil.

at the leading edge led to slight smearing of the shock waves, causing jumps in pressure coefficient directly at the leading edge.) For the cubic airfoil, the theoretical results tend to overpredict the peaks in positive and negative pressure coefficient (errors of 19 and 45%, respectively), with a deviation in the trailing-edge prediction. These trends are all believed to be from the small-disturbance assumptions inherent in the local linearization method.

A subsonic solution is shown in Fig. 5 for a Mach number of 0.76 for the parabolic arc and 0.65 for the cubic centerline. These Mach numbers correspond to roughly the lower critical Mach number on the geometries. Plotted in Fig. 5 are the viscous, computational solutions from TURNS for both a full airfoil and a half airfoil, along with the theoretical results predicted using Eq. (6) and the constant C_p alternative discussed earlier. For the parabolic arc, the half-airfoil solution is seen to be considerably different than the full airfoil shapes, showing the pressure leakage occurring due to the subsonic nature of the flowfield. Note that the half-airfoil solution is predicted remarkably well with the local linearization solution, despite the solution having been derived for full airfoils. For the cubic airfoil, the half- and full-airfoil computational solution show much better agreement, tending to deviate near the trailing edge.

The pressure distribution predicted by theory [Eq. (6)] on the parabolic airfoil is seen to give accurate predictions of the peak negative pressure on the geometry (error under 1%), but deviates for the leading and trailing edges due to a logarithmic term in the solution of Eq. (7). The cubic airfoil has the opposite trend: good predictions at the leading and trailing edges (with a maximum error compared to the full airfoil of under 18%), with an overprediction in negative peak pressure in the midsection (55%). Shown with the solution to Eq. (6) is the solution assuming constant C_p in the region where the bracket term of Eq. (6) is negative. Although the qualitative trend of pressure is not matched, quantitatively, the constant C_p assumption substantially reduces the error in the quantitative prediction of pressure (maximum error 40%).

A sonic solution is shown in Fig. 6 for the parabolic arc and the cubic centerline. Also shown are computational solutions for the half and full airfoil as well as experimental results from Michel et al.[20] for the full parabolic-arc airfoil. For the parabolic airfoil, good agreement is found between the theory [Eq. (8)], the computational results, and the experimental findings with an error in pressure of under 15% for the majority of the airfoil, excluding the leading edge. The full- and half-airfoil solutions are quite close (with a difference in C_p of under 0.07 for the majority of the airfoil, excluding the leading edge), showing that the lower flowfield is rather immune to communication from the upper surface.

For the cubic airfoil, the intersection point for Eq. (10) selected between the sonic and subsonic spline was the end of the linear section of the geometry. Good agreement is found between the theory and the computational results for the mid- and rear sections of the geometry, where the error in peak negative pressure coefficient is under 13%. At the leading edge, Eq. (10) correctly predicts the qualitative trend of the solution, but overpredicts the pressure by between 25 and 50% compared to the half- and full-airfoil solutions.

Axisymmetric Results

The local linearization method for axisymmetric geometries was applied to the parabolic-arc and cubic centerline shape described earlier. The supersonic, subsonic, and sonic pressure distributions are shown in Figs. 7, 8, and 9, respectively, where the negative pressure coefficient in the positive y direction is used. Also plotted in Figs. 7–9 are computational results calculated using OVERFLOW.[21] OVERFLOW is a thin-layer, Navier–Stokes solver that is capable of integrating multiple overset grids. The hyperbolic grid contained 100 points in the streamwise wraparound direction, 45 points in the direction normal to the surface, and 24 points in the azimuthal direction. The grid was extended a distance of 10 vehicle lengths from the surface of the geometry in all directions. Turbulence

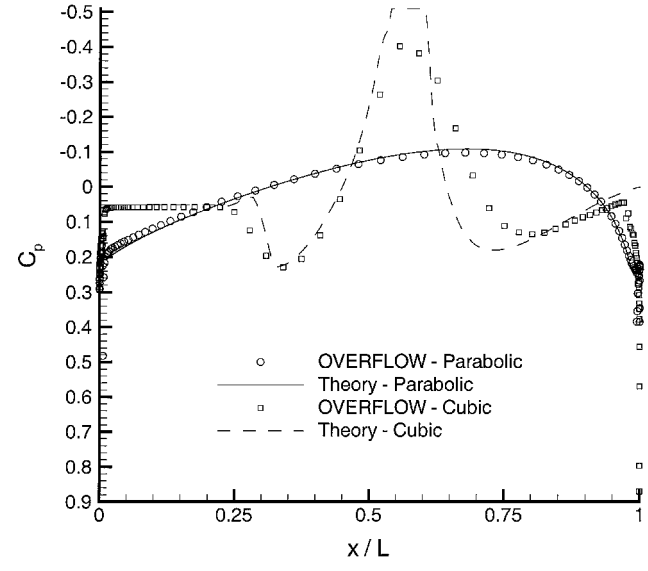

Fig. 7 Pressure distribution on parabolic and cubic body of revolution, $M_\infty = 1.21$.

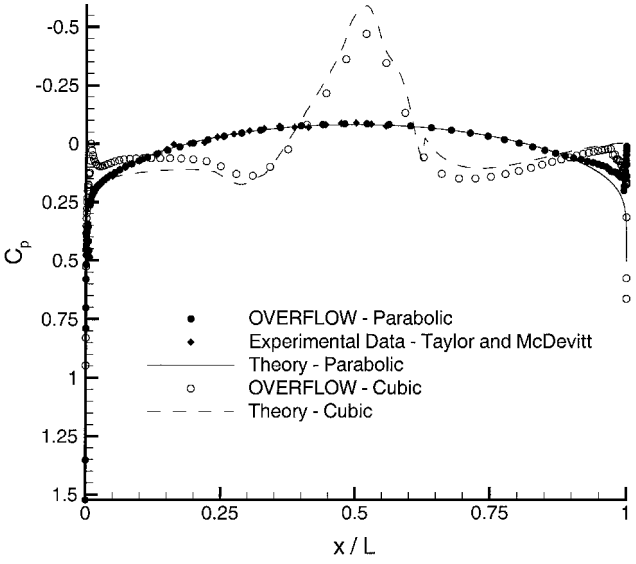

Fig. 8 Pressure distribution on parabolic and cubic body of revolution, $M_\infty = 0.8$.

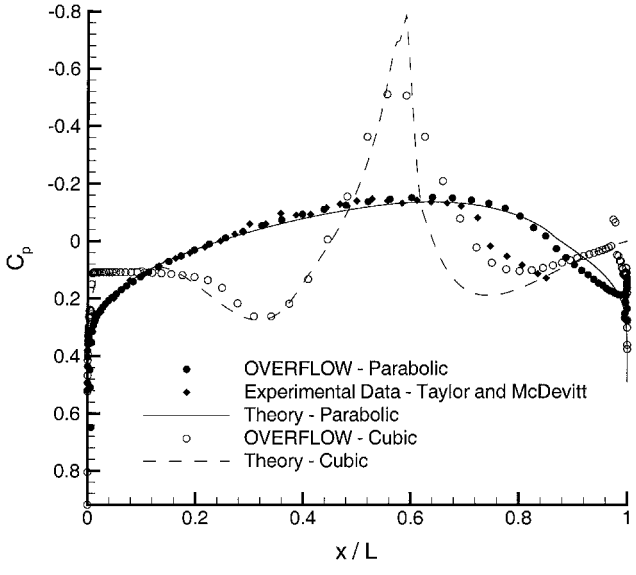

Fig. 9 Pressure distribution on parabolic and cubic body of revolution at sonic velocity.

was modeled in these computational solutions using the Baldwin–Lomax model[19] (same as used in the two-dimensional solutions). All viscous solutions were solved with a turbulent Reynold's number of 6×10^6 (the same as the two-dimensional solutions). Additionally, experimental data on the parabolic-arc profile[22] are provided for the subsonic and sonic solutions.

Supersonic solutions for the parabolic and cubic bodies of revolution are shown in Fig. 7 for a Mach number of 1.21 (corresponding to roughly the upper critical Mach number on these geometries). Plotted in Fig. 7 are the viscous, computational solutions from OVERFLOW along with the results from numerical integration of Eq. 13 (labeled theory). For the parabolic body of revolution, excellent agreement was found between the theory and computational solution, with a difference in peak negative pressure coefficient of 0.01 and an error at the leading edge of around 10%.

Details of the methodology used to solve the supersonic theoretical solution for the cubic airfoil may be found in Ref. 6. Figure 7 shows that the theoretical solution for the cubic geometry matches well with the computational results at the leading and trailing edges, with a C_p difference of 0.007 at the leading edge (Taylor–Maccoll region) and a difference in C_p of 0.07 at the trailing edge. The largest error occurs in the region where the two cubic sections intersect (corresponding to the region of minimum pressure coefficient). The error in peak negative pressure coefficient was around 30%. This error is largely attributed to the geometry to be solved. As stated earlier, the original geometry was designed to have continuous slope, not continuous third derivatives. However, when the limitations of the theory and the assumptions involved in finding the solution are considered, the theory does an acceptable job of modeling the flow.

Subsonic solutions for the parabolic and cubic bodies of revolution are shown in Fig. 8 for a Mach number of 0.8 (corresponding to roughly the lower critical Mach number on these geometries). Plotted in Fig. 8 are the viscous, computational solutions from OVERFLOW along with the results from numerical integration of Eq. 16 (labeled theory) and experimental data from Taylor and McDevitt[22] for a parabolic-arc body. For the parabolic body, excellent agreement is found in comparing both the computational and experimental results, with a difference in peak negative pressure coefficient of 0.0075, an error of under 6% in pressure coefficient near the leading edge, and an error in pressure coefficient of around 50% near the trailing edge (where flow separation affects the computational solution).

Details of the methodology used to solve the subsonic theoretical solution for the cubic airfoil may be found in Ref. 6. The solution, in general, is in good agreement with the computational results, with an error along the leading edge of a factor of two, and an error in the peak negative pressure region of about 27%. Note that as freestream Mach number decreases, the theoretical solution to the peak negative pressure region shows more error in comparison to the computational results. This is a direct consequence from the analytical geometry first assumed and may be mitigated with a smoother shape.

Sonic solutions for the parabolic and cubic bodies of revolution are shown in Fig. 9. Plotted in Fig. 9 are the viscous, computational solutions from OVERFLOW, along with the results from numerical integration of Eq. (18), and experimental data from Taylor and McDevitt[22] for a parabolic arc body. Again, for the parabolic body, good agreement is found between the theory, the computational solution, and the experimental results, with an error in peak negative pressure coefficient of around 10%. The largest discrepancy between the results is found on the rear portion of the object, where shock/boundary–layer interactions are causing flow separation. The sudden rise in pressure in the experimental results is due to the presence of a sting to hold the geometry in the wind tunnel. This effect is not modeled in the computational results nor in the theory presented.

Details of the methodology used to solve the sonic theoretical solution for the cubic airfoil may be found in Ref. 6. The resulting sonic theoretical solution on the cubic geometry is shown as theory in Fig. 9. The forward portion of the geometry is predicted well (error under 20%), with the largest error occurring near the maximum and minimum slope regions (35 and 55%, respectively). The rearward portion of the geometry demonstrates the same tendencies as seen in Fig. 7. The maximum error occurs in the region where the triple derivative in cross-sectional area has the largest deviations (errors over a factor of 10). Again, this error is attributable to the geometry selected and may be mitigated by selecting a smoother solution.

Application to Vehicle Fuselage

Solution of a vehicle geometry similar to that shown in Fig. 1 commences by eliminating the engine midline of the vehicle. The midline (where the compression ramps and engine are located) was eliminated to simplify the solution. Eliminating the engine section will result in an error in the pressure distribution due to interference effects, but will be considered negligible for this investigation. Where the engine section used to be, the fuselage is extended along the span direction to the centerline of the geometry. The resulting geometry is shown in Fig. 10. (See Ref. 6 for details on the geometry shown in Fig. 10.)

The flowfield on the vehicle will be solved by taking longitudinal slices in the freestream direction of the vehicle (Fig. 10) and then solving the two-dimensional and axisymmetric pressure distributions on each slice. After the vehicle has been solved assuming two-dimensional and axisymmetric flow, the solutions will be combined

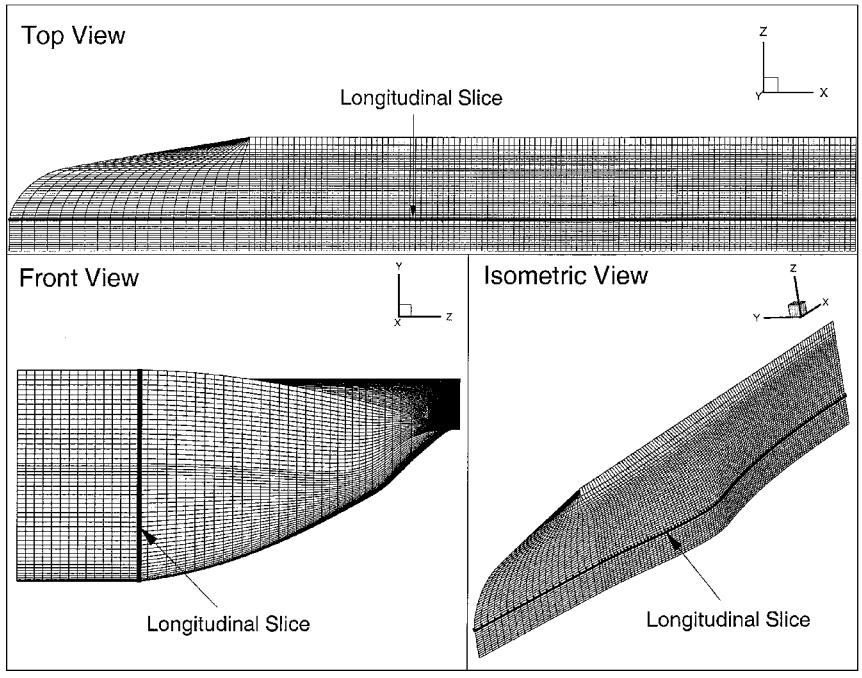

Fig. 10 Bottom surface geometry and longitudinal slice used in solving vehicle pressure distribution.

together. These solutions are then compared to an inviscid CFD solution over the three-dimensional, full vehicle (bottom surface replaced with the geometry in Fig. 10) for three Mach numbers: 0.65, 1, and 1.65. The subsonic and supersonic Mach numbers are the sub- and supercritical Mach numbers on the two-dimensional geometry. It is assumed that for the subsonic and supersonic solutions, there is no transition through Mach 1.

The inviscid theory will be compared to an inviscid, three-dimensional CFD solution for validation. Thus, viscous effects (which will be significant) are neither modeled nor validated. Also, this method does not account for crossflow, that is, flow in the spanwise direction, nor has it been applied to anything other than zero angle of attack.

The three-dimensional, inviscid, full-vehicle CFD solution was calculated using OVERFLOW.[21] Symmetric boundary conditions were used to solve the flowfield over half of the vehicle. OVERGRID[23] was used to generate an overset mesh about the three-dimensional object. The computational grids consisted of an inner hyperbolic grid generated about the geometry and an outer box grid generated to extend the far-field boundary. The inner hyperbolic grid had dimensions of 46 points in the spanwise wraparound direction, 279 points in the streamwise wraparound direction (including 104 points in the wake region), and 39 points in the direction normal to the surface. The inner grid was extended to a distance of one vehicle length from the surface of the geometry. The outer box grid had dimensions of $65 \times 61 \times 32$ points and was extended to a distance of over 10 vehicle lengths from the surface of the geometry.

Ultimately, it would be desirable to combine the two-dimensional and the axisymmetric solution together to predict the pressure profile on the full vehicle. The simplest way of combining the two solutions would be an average of the two results at each solution point on the geometry. This approach was taken for this investigation. A more rigorous way of blending the two solutions together would be to determine where on the vehicle the flow would behave more in a two-dimensional sense and where on the vehicle the flow would behave more in an axisymmetric sense. With this in mind, a proposed combination of the results based on local surface curvature would be

$$C_{p_{sp}} = C_{p_{axi}}(h_{max}/R_{loc})^n + C_{p2D}[1 - (h_{max}/R_{loc})^n] \qquad (20)$$

where n is an exponential value to be determined and R_{loc} is the local radius of curvature in the azimuthal plane. It is most likely that no single combination exists that will accurately predict the full-vehicle pressure profile for a wide range of geometries. However, the blending may be applicable for geometries that are similar to one another, such as waverider-based vehicle geometries.

Validation

The results of applying the two-dimensional and axisymmetric solutions to the full-vehicle fuselage by taking longitudinal slices will now be discussed. On the lower surface, four analytical solutions will be compared (depending on Mach number) with the inviscid, three-dimensional, full-vehicle fuselage computational solution: a solution assuming that each slice on the vehicle behaves in a two-dimensional manner, a solution assuming that each slice on the vehicle behaves axisymmetrically, an average of the two-dimensional and axisymmetric solutions, and the combination result of Eq. (20) for supersonic flow only. For the upper surface, only the two-dimensional solutions will be compared to the computational results. Because the upper surface has an expansion, the surface goes below the $y = 0$ plane near the trailing edge. Thus, when a body of rotation is formed along the $y = 0$ plane, the resulting axisymmetric geometry is incorrect. All theoretical results presented took an average of 10 s or less of CPU time (per Mach number) on a Sun Ultra 10, compared to hours for each three-dimensional Euler CFD computational result.

Line contours of pressure coefficient on the bottom surface and nondimensionalized pressure on the top surface of the vehicle at Mach 0.65 are presented in Figs. 11a and 11b, respectively. (Top surface pressure coefficients were not listed because their values were extremely small.) The forces on the lower and upper surfaces of the vehicle, as well as the percent error with respect to the CFD solution, are shown in Table 1. All forces are in square meters. (The form of pressure used to calculate the forces was p/p_∞.) The drag force D is the pressure force on the front side of the vehicle fuselage, and the thrust force T is the pressure force on the rear side of the vehicle.

The subsonic results on the lower surface assuming two-dimensional flow, axisymmetric flow, and an average of the two are compared to the computational solution for pressure coefficient in Fig. 11a. In general, all three solutions model both the trends and magnitudes of the pressure on the vehicle, shown by comparing the force results in Table 1. The maximum percent error for any of the methods is -3.9% for the two-dimensional drag force. The axisymmetric solution does the best job of modeling the forces on the vehicle (maximum error of 1.1%). The averaged solution does

Table 1 Forces on the vehicle fuselage[a]

	Bottom					Top		Total		
Forces	Two dimensional	Axisymmetric	Average	Spline (Eq. 20)	CFD	Two dimensional	CFD	Two dimensional	Axisymmetric	CFD
					$M_\infty = 0.65$					
L	717	741	729	——	737	−743	−740	−26	−2	−3
D	34.5	36.3	35.4	——	35.9	2.6	2.6	0.2	0.5	0.2
T	36.0	37.5	36.7	——	37.3	0.9	1.0	——	——	——
% L	−2.7	0.5	−1.1	——	——	0.4	——	767	−33.3	——
% D	−3.9	1.1	−1.4	——	——	0	——	0	150	——
% T	−3.5	0.5	−1.6	——	——	−10	——	——	——	——
					$M_\infty = 1$					
L	673	755	714	——	721	−737	−727	−64	18	−6
D	45.5	39.2	42.3	——	37.3	2.4	2.5	26.4	5.1	6.4
T	20.6	35.6	28.1	——	32.5	0.9	0.9	——	——	——
% L	−6.7	4.7	−1.0	——	——	1.4	——	967	−400	——
% D	22	5.1	13	——	——	−4	——	313	−20	——
% T	−37	9.5	−14	——	——	0	——	——	——	——
					$M_\infty = 1.65$					
L	761	759	760	763	707	−748	−744	13	11	−37
D	51.6	42.1	46.8	50.7	42.8	2.7	2.6	29.3	11.4	19.3
T	24.0	32.5	28.3	25	25.1	0.9	1.0	——	——	——
% L	7.6	7.4	7.5	7.9	——	0.5	——	−135	−130	——
% D	20.6	−1.6	9.3	18.5	——	3.8	——	51.8	−41	——
% T	−4.4	30	12.8	−0.4	——	−10	——	——	——	——

[a]Square meters.

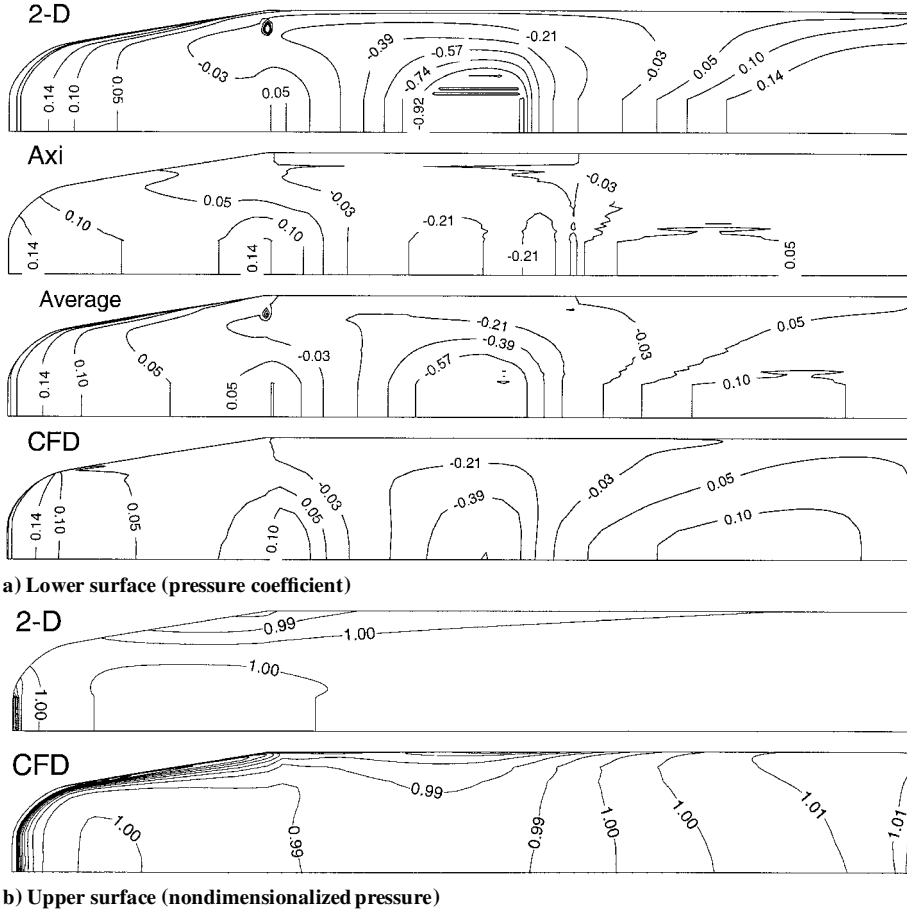

a) Lower surface (pressure coefficient)

b) Upper surface (nondimensionalized pressure)

Fig. 11 Pressure distribution on lower and upper surface of vehicle fuselage, M_∞ = 0.65.

the best job of modeling the overall pressure trends on the vehicle, especially the rear portion of the vehicle, where both the magnitude and the distribution are seen to be in excellent agreement. Note that using Eq. (20) to combine the two-dimensional and axisymmetric solution resulted in an "optimal" value of 0 for the exponent n (corresponding to purely axisymmetric flow).

The subsonic results on the upper surface assuming two-dimensional flow are compared to the computational solution for nondimensionalized pressure in Fig. 11b. In general, the upper surface of the geometry has very little pressure variation (varying by ±1% over the majority of the fuselage). The only significant variation in pressure occurs at the leading edge because of the flow expansion from the lower to the upper surface. The two-dimensional model captures the quantitative trends very well, but tends to be qualitatively less accurate near the trailing edge of the fuselage. The forces on the upper surface are compared to the CFD solution in

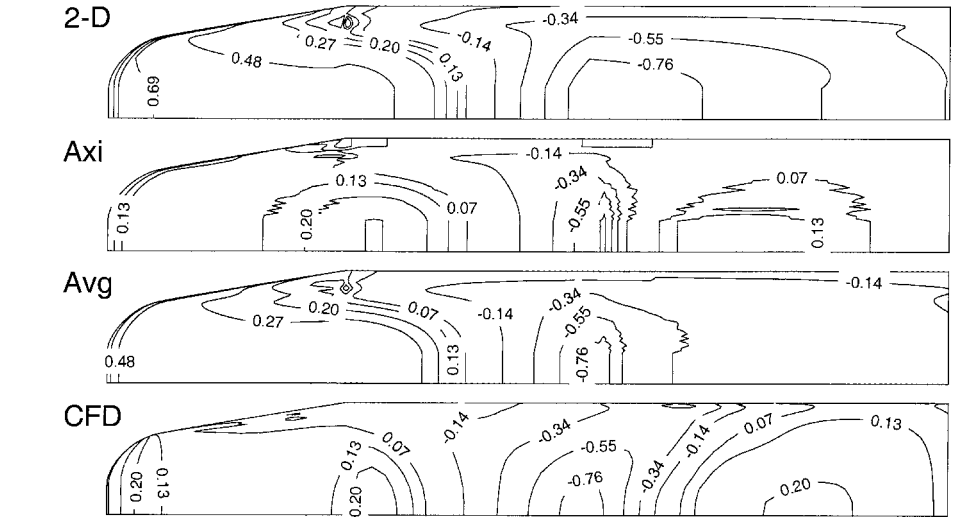

a) Lower surface (pressure coefficient)

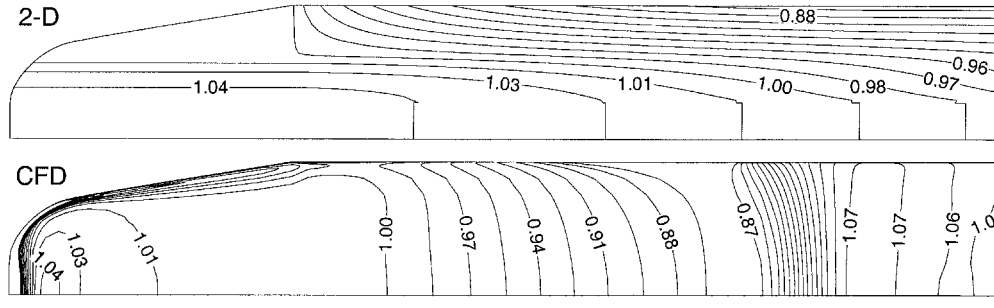

b) Upper surface (nondimensionalized pressure)

Fig. 12 Pressure distribution on lower and upper surface of vehicle fuselage, $M_\infty = 1$.

Table 1. The maximum error for all forces calculated on the upper surface was −10% for the thrust. However, when it is observed that the thrust is approximately 0.1% of the lift on the upper surface, this error is not significant.

The sonic results on the lower surface assuming two-dimensional flow, axisymmetric flow, and an average of the two are compared to the computational solution for pressure coefficient in Fig. 12a. Overall, the theory predicts the pressure distribution over the subsonic vehicle better than the sonic vehicle. The maximum percent error in force prediction was found to be −37% for the two-dimensional solution. In general, the two-dimensional solution was found to be a poor prediction of the vehicle flowfield, overpredicting the forebody region by over a factor of three and underpredicting the rear portion of the vehicle by about the same.

The best force prediction came from the axisymmetric solution, where the maximum percent error in force was 9.5% for the thrust. This is not a surprising result because the area rule uses an equivalent axisymmetric geometry to find the drag force. When the pressure profiles are compared, the axisymmetric solution models the forward portion of the geometry quite well (error in drag of 5.1%) and tends to underpredict the rear portion of the vehicle (shown by the thrust calculation and Fig. 12a). The averaged solution resulted in the lowest error in lift prediction of −1.0%, but was off for the drag by 13% and the thrust by −14%. Note that using Eq. (20) to combine the two-dimensional and axisymmetric solution resulted in an optimal value of 0 for the exponent n (corresponding to purely axisymmetric flow).

The sonic results on the upper surface assuming two-dimensional flow are compared to the computational solution for nondimensionalized pressure in Fig. 12b. The shock on the upper surface is clearly identifiable, with a compression ratio of about 1.2. The analytical model is found to be a poor predictor of the qualitative trends on the upper surface, but gives rough estimations of the quantitative forces on the upper surface. The flowfield solution on the upper surface is affected by the pressure leakage occurring at the leading edge from the lower surface. Hence, the analytical model (which assumes no interaction from the lower surface) will not be able to predict the trends observed in Fig. 12b. From Table 1, the maximum error in the forces calculated on the upper surface was −4% for the drag force. However, considering that the drag force is 0.3% of the lift force, this error is not significant.

The supersonic results on the lower surface assuming two-dimensional flow, axisymmetric flow, an average of the two, and the combination described by Eq. (20) ($n = 0.4$) are compared to the computational solution for pressure coefficient in Fig. 13a. The maximum error found was 30% error for the axisymmetric thrust calculation. The minimum error found was −0.4% for the thrust prediction using Eq. (20). All methods predicted lift to within 8%, with the axisymmetric solution yielding the best result with 7.4%. The two-dimensional solution again overpredicts the forebody region of the vehicle, with an error in drag prediction of 20.6%; however, the thrust prediction was to within −4.4%. The axisymmetric solution predicted the drag to within −1.6%, but overpredicted the thrust. The average solution yields a maximum error of 12.8% for the thrust calculation and a minimum error of 7.5% for the lift calculation. It is suggested that the best means of predicting the forces on the lower surface of the supersonic vehicle is to use any of the lift predictions, the drag prediction from the axisymmetric solution, and the thrust prediction from the two-dimensional or the combination solutions.

The supersonic results on the upper surface assuming two-dimensional flow are compared to the computational solution for nondimensionalized pressure in Fig. 13b. Except near the leading and trailing edge, the computational result predicts a pressure variation of approximately ±5%. This agrees well with the analytical result, which also predicts pressure variations of approximately ±5%. Two features on the computational solution are not predicted with the analytical model: the expansion occurring on the leading edge of the forebody and the shock occurring at the trailing edge of the

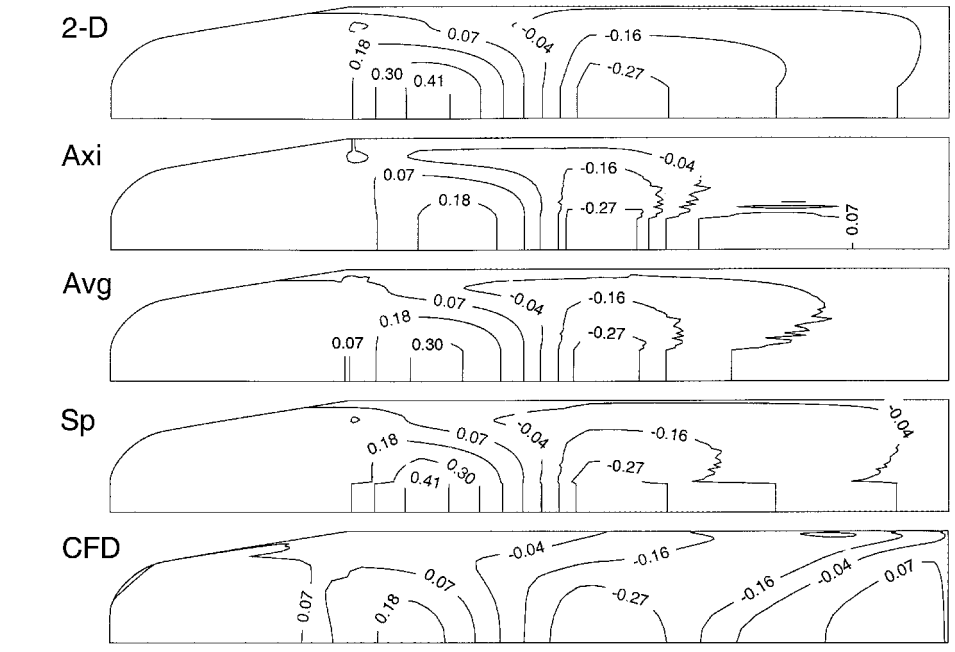

a) Lower surface (pressure coefficient)

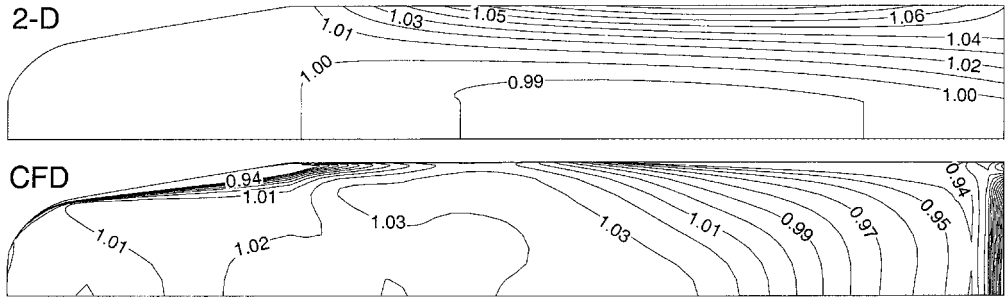

b) Upper surface (nondimensionalized pressure)

Fig. 13 Pressure distribution on lower and upper surface of vehicle fuselage, $M_\infty = 1.65$.

vehicle. The expansion is not predicted due to the assumption of zero crossflow. The trailing-edge shock is due to the flow exiting the lower surface; thus, the model will not predict this trend because it assumes no flow communication between the lower and upper surface. From Table 1, the maximum error in force prediction was −10% for the thrust calculation. However, the magnitude of the thrust is very small (~0.1% of the lift) so that the error is determined to not be significant.

The total lift and drag on the vehicle using the two-dimensional and axisymmetric modeling (where the upper surface is solved using the two-dimensional method) is compared to the computational solutions in Table 1. For the subsonic results, the percent error in net lift prediction was over 700% for the two-dimensional modeling and over 30% for the axisymmetric modeling. These percentage errors are indeed quite high. However, on inspection of the net lift predicted by the computational solutions, the lift on this geometry is very small (approximately 0.3% of the average lift force on the lower and upper surface). The analytical predictions for lift, compared to the average lift force, were found to be 3.5% for the two-dimensional modeling and 0.2% for the axisymmetric modeling. Thus, although the analytical methods do not quantitatively predict the correct value of lift, they do qualitatively predict that there will be very little lift on this geometry. This argument holds true for the rest of the lift force errors reported in Table 1. However, the analytical methods are found to better predict the net drag on the vehicle, but still these errors are a bit high.

An important result from the numerical and analytical results reported in Table 1 is the inability of the vehicle fuselage to produce sufficient, positive lift at low speeds. In fact, this class of vehicle geometry in general has poor lift performance for Mach numbers less than 3 and for angles of attack as high as 6 deg (Ref. 24). Thus, the fuselage will either have to be inclined at a relatively high angle of attack, or some form of lift augmentation such as wings, canards, or thrust from the engine will be needed to obtain significant lift for takeoff and low-speed flight.

Conclusions

A method for rapidly predicting the inviscid, transonic, aerodynamic performance of a high-speed, slender hypersonic fuselage has been presented. Though the example chosen is a waverider-derived form, the actual waverider properties are irrelevant in the low-speed region where this study was focused, and the method should be applicable to any general slender hypersonic lifting body form. The method calculates the pressure distribution over the surface (ignoring interference effects from the engine) in CPU times of approximately 10 s using a Sun Ultra 10. The Spreiter and Alksne method of local linearization[14,15] was used to reduce the two-dimensional and axisymmetric transonic, small-perturbation, velocity potential equations into analytical and nonlinear ODEs, respectively. These equations are then solved along longitudinal slices of the vehicle geometry to predict the pressure distribution on a three-dimensional vehicle. The theoretical results were then compared to an inviscid, three-dimensional, computational solution over the vehicle geometry.

In general, the methodology developed herein accurately predicted the forces on the lower and upper surface of the vehicle fuselage. However, because of the low values of net forces on the fuselage, larger fractional errors were found when the analytical results for the lower and upper surface were combined together.

Overall, for the CPU time constraints imposed, the method yields results that will be useful for initial design phase studies and/or studies that involve many vehicle geometry iterations (such as trajectory performance or optimization).

A major conclusion reached through the analytical and computational analyses of the fuselage showed that this class of vehicle geometries perform poorly in the generation of low-speed lift. Lift augmentation in the form of wings, canards, or thrust from the engine will be needed to provide sufficient lift in the subsonic through low supersonic regime.

Acknowledgments

This research was supported by NASA John H. Glenn Research Center at Lewis Field. Technical Monitor for this research was Donald Palac, the support of whom is greatly appreciated. Thanks also go to James Reuster and Ryan Starkey of the University of Maryland for their extensive assistance in acquiring the computational solutions presented.

References

[1]Tarpley, C., "The Optimization of Engine-Integrated Hypersonic Waveriders with Steady State Flight and Static Margin Constraints," Ph.D. Dissertation, Dept. of Aerospace Engineering, Univ. of Maryland, College Park, MD, 1995.

[2]O'Neill, M. K. L., "Optimized Scramjet Engine Integration on a Waverider Airframe," Ph.D. Dissertation, Dept. of Aerospace Engineering, Univ. of Maryland, College Park, MD, 1992.

[3]Takashima, N., "Optimization of Waverider-Based Hypersonic Vehicle Designs," Ph.D. Dissertation, Dept. of Aerospace Engineering, Univ. of Maryland, College Park, MD, 1997.

[4]Starkey, R. P., "Investigation of Air-Breathing, Hypersonic Missile Configurations Within External Box Constraints," Ph.D. Dissertation, Dept. of Aerospace Engineering, Univ. of Maryland, College Park, MD, Oct. 2000.

[5]O'Brien, T. F., and Lewis, M. J., "Rocket-Based Combined-Cycle Engine Integration on an Osculating Cone Waverider Vehicle," *Journal of Aircraft*, Vol. 38, No. 6, 2001, pp. 1117–1123.

[6]O'Brien, T. F., "RBCC Engine-Airframe Integration on an Osculating Cone Waverider Vehicle," Ph.D. Dissertation, Dept. of Aerospace Engineering, Univ. of Maryland, College Park, MD, Aug. 2001.

[7]Long, L. N., "Off-Design Performance of Hypersonic Waveriders," *Journal of Aircraft*, Vol. 27, No. 4, 1990, pp. 639–646.

[8]Strohmeyer, D., "Lateral Stability Derivatives for Osculating Cones Waveriders in Sub- and Transonic Flow," AIAA Paper 98-1618, April 1998.

[9]Vanhoy, D., "Low-Speed Wind Tunnel Testing of a Mach 6 Viscous Optimized Waverider," M.S. Thesis, Dept. of Aerospace Engineering, Univ. of Maryland, College Park, MD, 1988.

[10]Miller, R. W., and Argrow, B. W., Subsonic Aerodynamics of an Osculating Cones Waverider," AIAA Paper 97-0189, Jan. 1997.

[11]Hummel, D., Blaschke, R., Eggers, T., and Strohmeyer, D., "Experimental and Numerical Investigations on Waveriders in Different Flight Regimes," 21st International Council of the Aeronautical Sciences Congress, ICAS, Paper 2.11.3, 1998.

[12]Ferrari, C., and Tricomi, F., *Transonic Aerodynamics*, Academic Press, New York, 1968.

[13]Cole, J., and Cook, L. P., *Transonic Aerodynamics*, Elsevier Science, Amsterdam, 1986.

[14]Spreiter, J. R., and Alksne, A. Y., "Thin Airfoil Theory Based on Approximate Solution of the Transonic Flow Equation," NACA Rept. 1359, 1958.

[15]Spreiter, J. R., and Alksne, A. Y., "Slender-Body Theory Based on Approximate Solution of the Transonic Flow Equation," NASA TR R-2, 1959.

[16]Kreyszig, E., *Advanced Engineering Mathematics*, 7th ed., Wiley, New York, 1993, pp. 1040–1043.

[17]O'Brien, T. F., and Lewis, M. J., "RBCC Engine-Airframe Integration on an Osculating Cone Waverider Vehicle," AIAA Paper 2000-3823, July 2000.

[18]Srinivasan, G. R., and Baeder, J. D., "TURNS: A Free Wake Euler/Navier–Stokes Numerical Method for Helicopter Rotors," *AIAA Journal*, Vol. 31, No. 5, 1993, pp. 959–962.

[19]Baldwin, B. S., and Lomax, H., "Thin Layer Approximation and Algebraic Model for Separated Turbulent Flows," AIAA Paper 78-0257, Jan. 1978.

[20]Michel, R., Marchaud, F., and Le Gallo, J., "Étude des écoulements transsoniques autour des profils lenticulaires, a incidence nulle," ONERA Publ. 65, 1953.

[21]Buning, P. G., Jespersen, D. C., Pulliam, T. H., Chan, W. M., Slotnick, J. P., Krist, S. E., and Renze, K. J., "Overflow User's Manual," NASA Langley Research Center, 1998.

[22]Taylor, R. A., and McDevitt, J. B., "Pressure Distributions at Transonic Speeds for Parabolic-Arc Bodies of Revolution Having Fineness Ratios of 10, 12, and 14," NACA TN 4234, 1958.

[23]Chan, W. M., Chiu, I.-T., and Buning, P. G., "User's Manual for the HYPGEN Hyperbolic Grid Generator and the HGUI Graphical User Interface," NASA TM 108791, 1993.

[24]O'Brien, T. F., and Lewis, M. J., "Transonic through Hypersonic Performance of an RBCC Engine-Airframe Integrated Vehicle," AIAA Paper 2001-1919, April 2001.